Structures 87 (2026) 111617

Contents lists available at ScienceDirect

Structures

journal homepage: www.elsevier.com/locate/istruc

Characterization of the nonlinear rocking dynamics of dual isolated asymmetric rigid blocks

Lorenzo Amoroso, Manuel Ferretti*, Angelo Di Egidio

Department of Civil, Construction-Architectural and Environmental Engineering, University of L'Aquila, 67100 L'Aquila, Italy

ARTICLE INFO

Keywords:
Asymmetric rigid block
Eccentricity
Horizontal and vertical base isolation
Overturning mechanism
Seismic performance

ABSTRACT

The rocking response of rigid bodies has been extensively studied in Mechanics and Civil Engineering, especially following the foundational work of Housner. While prior research has primarily examined symmetric blocks, structures that react the same way to excitations in either direction, many practical configurations involve asymmetry, where the centers of mass and geometry do not coincide. This asymmetry results in direction-dependent responses under dynamic loading. This study explores the seismic behavior of asymmetric rigid blocks supported by a dual isolation system, featuring both horizontal and vertical components, with particular emphasis on characterizing and understanding their nonlinear dynamic response. The governing equations of motion are derived, accounting for both rocking and full-contact phases, as well as uplift and impact conditions. The horizontal isolation is modeled using a Bouc-Wen hysteretic formulation, while the vertical isolation system is represented with a Kelvin-Voigt viscoelastic model.

The first part concerns the seismic analysis of the system. As base excitation, three earthquake horizontal and vertical records are selected accounting for their spectral content and PGA. The results are arranged in rocking maps and comparisons among the systems referring to symmetric rigid blocks and those referring to asymmetric blocks with increasing eccentricity are performed to examine the role of the asymmetry of blocks protected with the dual base isolation. Results show that vertical isolation, when combined with horizontal isolation, enhances the block's ability to remain in full-contact compared to the case with horizontal isolation alone.

The second part focuses on the overturning mechanisms exhibited by asymmetric rigid blocks equipped with the previously discussed dual base isolation system. To this end, the system is subjected to horizontal and vertical impulsive one-sine base accelerations, and the resulting overturning spectral maps are constructed. The analysis uncovers previously unidentified overturning modes specific to dual-isolated asymmetric blocks.

1. Introduction

To study the dynamic response of rocking bodies, it is crucial to adopt suitable mechanical models. A foundational approach was developed with the inverted pendulum model (IPM), first proposed in [1], which describes the in-plane motion of a rectangular rigid block subjected to rocking. This formulation captures the essential features of planar rocking for symmetric rigid blocks, intentionally neglecting effects such as sliding and detachment phases. Despite its simplifications, the IPM has become a cornerstone in the field due to its ability to qualitatively capture the fundamental dynamics. It has been extensively applied in subsequent research to assess the seismic behavior of rigid bodies [2–5]. Over time, additional models have been introduced to incorporate more complex mechanisms, including slip and lift-off, extending the original framework to a broader range of dynamic phenomena [6–8].

Subsequent contributions considered imperfections in block geometry and base contact conditions [9], and provided analytical formulations for overturning based on energy considerations [10]. More refined intensity measures tailored to rocking dynamics were proposed in [11], and advanced three-dimensional models incorporating impact and uplift effects were developed in [12–14], enhancing the realism of rocking simulations.

In parallel, efforts have been made to reduce the vulnerability of rigid blocks through passive control techniques. The use of combined strategies involving tuned mass dampers, inerters, and hysteretic elements has been studied in detail [15–20], demonstrating their effectiveness

* Corresponding author.
Email addresses: lorenzo.amoroso@univaq.it (L. Amoroso), manuel.ferretti@univaq.it (M. Ferretti), angelo.diegidio@univaq.it (A. Di Egidio).

https://doi.org/10.1016/j.istruc.2026.111617
Received 17 November 2025; Received in revised form 12 February 2026; Accepted 7 March 2026
Available online 14 March 2026

in mitigating overturning during seismic events. A promising approach to improve seismic performance involves the application of base isolation to rigid blocks. Numerical and analytical investigations on isolated configurations have shown substantial reductions in rocking intensity and overturning probability [21,22]. Additional studies have focused on the efficiency of base-isolated systems under near-fault or pulse-type excitations [23]. The combined use of horizontal and vertical isolation is explored in [24], where improved energy dissipation and enhanced stability are reported for symmetric rigid blocks. Also semi-active and active control techniques have been employed by using different control strategies and algorithms [25–28].

The dynamics of asymmetric rigid blocks on fixed bases, which differ significantly from symmetric configurations due to mass eccentricity and non-uniform geometry, have also garnered attention due to their complex behavior under seismic excitation. A detailed characterization of overturning mechanisms under impulsive one-sine excitation is provided in [29], while control-oriented models and mitigation approaches are proposed in [22,30,31]. These studies reveal the increased sensitivity of asymmetric systems to combined horizontal and vertical motions, as well as the challenges associated with restoring stability post-excitation.

This work builds upon previous investigations concerning the seismic behavior of symmetric rigid blocks with horizontal base isolation and asymmetric blocks on fixed supports, aiming to integrate these two lines of research within a comprehensive modeling framework. A dynamic model is formulated to accurately describe the motion of asymmetric rigid blocks resting on a dual-isolated base, working both in horizontal and vertical directions, explicitly incorporating the eccentricity between the center of mass and the geometric center. The analysis focuses on non-sliding bodies undergoing full-contact and rocking motions only. The equations of motion are derived for general asymmetric configurations, with the uplift and impact conditions explicitly incorporated into the model. Due to geometric asymmetry, the dynamic response exhibits directional dependence: the rocking, uplift, and impact behavior differs based on the side from which rocking initiates, resulting in distinct kinematic and dynamic features for leftward and rightward motion.

The proposed model is used to investigate the behavior of a set of representative rigid bodies subjected to both recorded earthquake ground motions and one-sine impulsive accelerations, considering both horizontal and vertical components. While real seismic records were employed to investigate the overall response of dual-isolated asymmetric blocks, the one-sine excitations were specifically used to study overturning mechanisms. Rocking and overturning spectral maps are developed to evaluate the sensitivity of the system to key parameters, such as the characteristic isolation periods and block eccentricity, under both seismic and impulsive loading conditions.

Results show that vertical isolation, when combined with horizontal isolation, enhances the asymmetric block's ability to remain in full-contact. Moreover, the analysis uncovers previously unidentified overturning mechanisms specific to dual-isolated asymmetric blocks and provides a deeper insight into their nonlinear dynamic behavior.

The paper is organized as follows. In Section 2, the mechanical model of dual-isolated asymmetric rigid blocks is derived. Section 3 presents the fixed and variable parameters used in the parametric analyses. In Section 4, the seismic response of the blocks is investigated under recorded earthquake ground motions, while Section 5 addresses the determination of overturning spectra under one-sine pulse excitations. Finally, Section 6 summarizes the main conclusions and key findings of the study.

2. Mechanical model

The mechanical configuration under consideration, potentially representative of valuable artworks or sensitive equipment, comprises an asymmetric rigid block positioned on a base that is isolated in both the horizontal and vertical directions.

The block is characterized by a generic geometry and has mass M. Its base spans $2B$, while the height of the center of mass C is H (refer to Fig. 1(a). The block also exhibits a constant depth D, perpendicular to the x-y plane. Notably, the center of mass C does not align with the geometric center G, which is defined as the point located at the same vertical level as the center of mass and symmetrically positioned between the rocking vertices. The horizontal offset between C and G is termed the eccentricity e (see again Fig. 1(a)).

To quantify this asymmetry, a non-dimensional parameter $\varepsilon = \frac{e}{B} \times 100$ is introduced. When $\varepsilon = 0$, the center of mass coincides with the geometric center; when $\varepsilon = 100\%$, the center of mass lies on the vertical line passing through the right corner of the block's base. Both e and ε may be either positive or negative: a positive value implies that C is located to the right of G, while a negative value indicates a shift to the left.

The isolation system consists of two plates with masses m_h and m_v allowing motion in the horizontal and vertical directions, respectively. These plates are interconnected and linked to the ground through energy-dissipating elements (see Fig. 1a). The plates are separated vertically by a distance h and have a thickness equal to $2s$.

Assuming the block is slender, i.e., that the slenderness ratio $\lambda = H/B$ is sufficiently large, two primary motion regimes are possible:

(a) *Full contact:* the block remains in continuous contact with the base without initiating any rotation;
(b) *Rocking:* the block rotates about one of its bottom corners, either ℓ or r (see Fig. 1b).

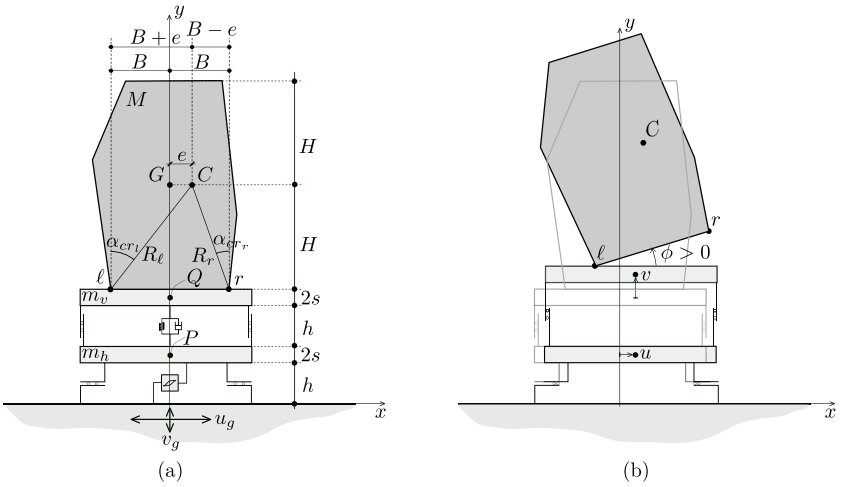

Fig. 1. Symmetric rigid block: (a) Geometrical characterization of the block; (b) Rocking around the left base vertex ℓ (positive Lagrangian parameters).

Although sliding could occur, where the block translates without rotating, this possibility is disregarded due to the assumed slenderness. In fact, most rigid block models in the literature neglect sliding for two reasons: (*i*) constraints often inhibit sliding, and (*ii*) when the slenderness $\lambda > 2$, the block tends to rock rather than slide [31].

Finally, $u_g = u_g(t)$ and $v_g = v_g(t)$ are the horizontal and vertical ground motions, where t is the time.

2.1. Full-contact equation of motion

In the full-contact phase, the displacements experienced by the centers of mass of the plates constituting the isolated base and the rigid body, denoted in Fig. 1(a) by P, Q, and C, respectively, are expressed as follows:

$$\mathbf{u}_P = \begin{pmatrix} u_g + u \\ v_g \\ 0 \end{pmatrix}, \qquad \mathbf{u}_Q = \begin{pmatrix} u_g + u \\ v_g + v \\ 0 \end{pmatrix}, \qquad \mathbf{u}_C^{FC} = \begin{pmatrix} u_g + u \\ v_g + v \\ 0 \end{pmatrix}, \tag{1}$$

where $u = u(t)$ and $v = v(t)$ are the Lagrangian parameters representing the horizontal and vertical displacements of the plates constituting the isolated base. Accordingly, the kinetic and potential energies are defined as:

$$T^{FC} = \frac{1}{2} m_h \, \dot{\mathbf{u}}_P \cdot \dot{\mathbf{u}}_P + \frac{1}{2} m_v \, \dot{\mathbf{u}}_Q \cdot \dot{\mathbf{u}}_Q + \frac{1}{2} M \, \dot{\mathbf{u}}_C^{FC} \cdot \dot{\mathbf{u}}_C^{FC}, \tag{2a}$$

$$U^{FC} = M \, g \, \mathbf{u}_C^{FC} \cdot \mathbf{j} + m_v \, g \, \mathbf{u}_Q \cdot \mathbf{j}, \tag{2b}$$

where $\mathbf{j} = (0, 1, 0)^T$ is the canonical unit vector along the y-axis. Consequently, the Lagrangian is defined as $L^{FC} := T^{FC} - U^{FC}$.

The virtual work of non-conservative forces is given by:

$$\delta W = F_h \, \delta u + F_v \, \delta v, \tag{3}$$

where F_h and F_v denote the horizontal and vertical restoring forces of the isolated base, respectively.

The Euler–Lagrange equations are therefore written as:

$$\frac{\mathrm{d}}{\mathrm{d}t}\left(\frac{\partial L^{FC}}{\partial \dot{u}}\right) - \frac{\partial L^{FC}}{\partial u} = F_h, \tag{4a}$$

$$\frac{\mathrm{d}}{\mathrm{d}t}\left(\frac{\partial L^{FC}}{\partial \dot{v}}\right) - \frac{\partial L^{FC}}{\partial v} = F_v, \tag{4b}$$

and, using the expressions previously introduced, read:

$$(M + m_h + m_v)(\ddot{u} + \ddot{u}_g) = F_h, \tag{5a}$$

$$(M + m_v)(\ddot{v} + \ddot{v}_g + g) = F_v. \tag{5b}$$

2.2. Rocking equations of motion

During the rocking phases about the corners ℓ and r, the displacements of points P and Q remain as defined in Eq. (1), while the displacement of point C is given by:

$$\mathbf{u}_C^{\ell,r} = \begin{pmatrix} \mp(B \pm e) + u + u_g \\ -H + v + v_g \\ 0 \end{pmatrix} + \begin{bmatrix} \cos\phi & -\sin\phi & 0 \\ \sin\phi & \cos\phi & 0 \\ 0 & 0 & 1 \end{bmatrix} \begin{pmatrix} \pm(B \pm e) \\ H \\ 0 \end{pmatrix}, \tag{6}$$

where $\phi = \phi(t)$ is the Lagrangian parameter describing the rocking rotation of the rigid body (see Fig. 1b).

The $\pm$ signs indicate the kinematic formulation associated with the rotation about either the left (ℓ) or right (r) corner of the base. Whenever a double sign $\pm(\cdot)$ or $\mp(\cdot)$ appears, it should be interpreted such that the upper sign corresponds to the motion about the left vertex ℓ, and the lower sign corresponds to the right vertex r. In these expressions, the first subscript or superscript must always align with the upper sign (left vertex), while the second aligns with the lower sign (right vertex). Accordingly, the kinetic and potential energies take the following forms:

$$T^{\ell,r} = \frac{1}{2} m_h \, \dot{\mathbf{u}}_P \cdot \dot{\mathbf{u}}_P + \frac{1}{2} m_v \, \dot{\mathbf{u}}_Q \cdot \dot{\mathbf{u}}_Q + \frac{1}{2} M \, \dot{\mathbf{u}}_C^{\ell,r} \cdot \dot{\mathbf{u}}_C^{\ell,r} + \frac{1}{2} J_C \, \dot{\phi}^2, \tag{7a}$$

$$U^{\ell,r} = M \, g \, \mathbf{u}_C^{\ell,r} \cdot \mathbf{j} + m_v \, g \, \mathbf{u}_Q \cdot \mathbf{j}. \tag{7b}$$

Here, J_C denotes the mass moment of inertia of the rigid block about its center of mass C.

The associated Lagrangians are defined as $L^{\ell,r} := T^{\ell,r} - U^{\ell,r}$, and the virtual work due to non-conservative forces remains as expressed in Eq. (3). The corresponding Euler–Lagrange equations can therefore be written as:

$$\frac{\mathrm{d}}{\mathrm{d}t}\left(\frac{\partial L^{\ell,r}}{\partial \dot{u}}\right) - \frac{\partial L^{\ell,r}}{\partial u} = F_h, \tag{8a}$$

$$\frac{\mathrm{d}}{\mathrm{d}t}\left(\frac{\partial L^{\ell,r}}{\partial \dot{v}}\right) - \frac{\partial L^{\ell,r}}{\partial v} = F_v, \tag{8b}$$

$$\frac{\mathrm{d}}{\mathrm{d}t}\left(\frac{\partial L^{\ell,r}}{\partial \dot{\phi}}\right) - \frac{\partial L^{\ell,r}}{\partial \phi} = 0. \tag{8c}$$

Substituting the expressions previously introduced, the equations become:

$$\begin{aligned}(M + m_h + m_v)(\ddot{u}_g + \ddot{u}) \mp M\,[(B \pm e)\cos\phi \mp H \sin\phi]\,\dot{\phi}^2 \\ - M\,[H\cos\phi \pm (B \pm e)\sin\phi]\,\ddot{\phi} = F_h,\end{aligned} \tag{9a}$$

$$\begin{aligned}(M + m_v)(g + \ddot{v}_g + \ddot{v}) - M\,[H\cos\phi \pm (B \pm e)\sin\phi]\,\dot{\phi}^2 \\ \pm M\,[(B \pm e)\cos\phi \mp H\sin\phi]\,\ddot{\phi} = F_v,\end{aligned} \tag{9b}$$

$$\begin{aligned}\left[J_C + M\left[(B \pm e)^2 + H^2\right]\right]\ddot{\phi} - M\cos\phi\left[H(\ddot{u}_g + \ddot{u}) \mp (B \pm e)(g + \ddot{v}_g + \ddot{v})\right] \\ - M\sin\phi\left[\pm(B \pm e)(\ddot{u}_g + \ddot{u}) + H(g + \ddot{v}_g + \ddot{v})\right] = 0.\end{aligned} \tag{9c}$$

2.3. Characteristics of the isolation devices

The behaviors of the horizontal and vertical devices within the isolating base differ from one another. Specifically, the restoring forces of the horizontal isolation system are described by the Bouc–Wen model [32], whereas those of the vertical isolation system follow the linear viscoelastic Kelvin–Voigt model [33]. According to these formulations, the restoring forces can be expressed as:

$$F_h = -\left[\psi \, k_h u + k_h u_y (1 - \psi) z + c_h \dot{u}\right], \tag{10a}$$

$$F_v = -\left(k_v v + c_v \dot{v}\right). \tag{10b}$$

In Eq. (10a), the coefficient ψ is the ratio between the post-yielding horizontal stiffness k_{hp} and the pre-yielding horizontal stiffness k_h, that is, $k_{hp} = \psi \, k_h$. The term u_y represents the yielding displacement. The case $\psi = 0$ corresponds to a perfectly elasto-plastic behavior of the horizontal connection devices, while $\psi = 1$ represents a perfectly elastic behavior. The variable $z = z(t)$ is the hysteretic internal variable that describes the post-yielding response and is evaluated by solving the following nonlinear first-order ordinary differential equation:

$$\dot{z} = \frac{\dot{u}}{u_y}\left[A_h - |z|^n \left(\beta_h + \gamma_h \, \mathrm{sign}(\dot{u} \cdot z)\right)\right]. \tag{11}$$

In Eq. (10b), k_v is the vertical elastic stiffness. The viscous damping coefficients c_h and c_v are defined by:

$$c_h = 2(M + m_h + m_v)\,\xi_h \, \omega_h, \tag{12a}$$

$$c_v = 2(M + m_v)\,\xi_v \, \omega_v, \tag{12b}$$

where the (conventional) natural frequencies of the isolation system are given by:

$$\omega_h = \sqrt{\frac{k_h}{M + m_h + m_v}}, \tag{13a}$$

$$\omega_v = \sqrt{\frac{k_v}{M + m_v}}, \tag{13b}$$

and ξ_h, ξ_v are the damping ratios associated with the horizontal and vertical isolation systems, respectively. In the following, $\xi_h = 0.05$ and $\xi_v = 0.10$ are assumed.

As is well known, the parameters of the Bouc–Wen model are functionally redundant. To eliminate this redundancy, the values $A_h = 1$ and $\beta_h = \gamma_h = 0.5$ are adopted. These assumptions reduce the Bouc–Wen model to a strain-softening formulation, in which mechanical quantities retain a clear physical interpretation. Under these conditions, the dimensionless hysteretic variable z is bounded within the interval $[-1, 1]$ (see, e.g., [34,35]). Finally, the exponential parameter n, which governs the abruptness of the transition between the elastic and post-elastic branches of the hysteretic model, is taken as $n = 2$.

2.4. Uplift conditions

Starting from the rest position, the transition from the full-contact phase to the rocking phase (about ℓ or r) may occur depending on the uplift conditions. These conditions are defined by comparing the overturning moments, associated with the horizontal acceleration of the isolated base and the horizontal seismic component, with the restoring moments, which instead depend on the gravitational acceleration, the vertical acceleration of the isolated base, and the vertical seismic component. The evaluation is made with respect to the rotation poles ℓ and r.

These conditions can be expressed through the following inequality (see Fig. 2):

$$\pm(\ddot{u} + \ddot{u}_g) > \frac{B \pm e}{H}(\ddot{v} + \ddot{v}_g + g). \tag{14}$$

If the inequality is satisfied using the plus sign, rocking initiates around ℓ; if the minus sign applies, rocking occurs around r.

2.5. Impact conditions

The impact conditions occur when the rocking angle ϕ becomes zero during the rocking motion around ℓ or r. Assuming that no bouncing phenomena occur and that the impact happens instantaneously, it is possible to determine the post-impact velocities by imposing the conservation of horizontal, vertical, and angular momentum. These read:

$$\left[\left(m_h\dot{\mathbf{u}}_P + m_v\dot{\mathbf{u}}_Q + M\dot{\mathbf{u}}_C^{r,\ell}\right)\cdot\mathbf{i}\right]_b = \left[\left(m_h\dot{\mathbf{u}}_P + m_v\dot{\mathbf{u}}_Q + M\dot{\mathbf{u}}_C^{\ell,r}\right)\cdot\mathbf{i}\right]_a, \tag{15a}$$

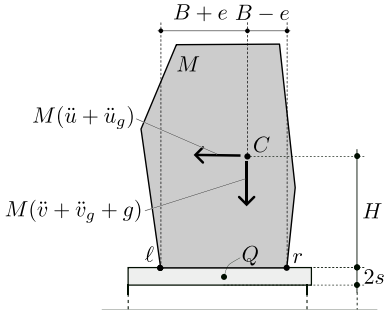

Fig. 2. Forces acting on the rigid block during the full-contact state.

$$\left[\left(m_v\dot{\mathbf{u}}_Q + M\dot{\mathbf{u}}_C^{r,\ell}\right)\cdot\mathbf{j}\right]_b = \left[\left(m_v\dot{\mathbf{u}}_Q + M\dot{\mathbf{u}}_C^{\ell,r}\right)\cdot\mathbf{j}\right]_a, \tag{15b}$$

$$\left[J_C\dot{\phi} + M(\mathbf{R}^{\ell,r}\times\dot{\mathbf{u}}_C^{r,\ell})\cdot\mathbf{k}\right]_b = \left[J_C\dot{\phi} + M(\mathbf{R}^{\ell,r}\times\dot{\mathbf{u}}_C^{\ell,r})\cdot\mathbf{k}\right]_a, \tag{15c}$$

where:

- The vectors $\mathbf{i} = (1,0,0)^T$ and $\mathbf{k} = (0,0,1)^T$ are the canonical unit vectors along the x and z axes;
- The terms on the left side of the equalities ($[\cdot]_b$) correspond to the *pre-impact* condition, while those on the right ($[\cdot]_a$) correspond to the *post-impact* condition;
- The vectors $\mathbf{R}^{\ell,r} = (\pm(B \pm e),\ H,\ 0)^T$ are the position vectors of the mass center C with respect to the poles (ℓ, r); the *plus* sign is taken if the sequence pre–post impact is $r \to \ell$, and *minus* otherwise.

In explicit form, if the pre–post impact sequence is $r, \ell \to \ell, r$, and denoting post-impact velocities with superscript "+" and pre-impact velocities with superscript "−", the post-impact velocities are:

$$\dot{u}^+ = \dot{u}^- - \eta_u^{\ell,r}\,\dot{\phi}^-, \tag{16a}$$

$$\dot{v}^+ = \dot{v}^- \mp \eta_v^{\ell,r}\,\dot{\phi}^-, \tag{16b}$$

$$\dot{\phi}^+ = \eta_\phi^{\ell,r}\,\dot{\phi}^-. \tag{16c}$$

The *restitution coefficients* are given as:

$$\eta_u^{\ell,r} = \frac{2B(B \pm e)HM^2m_v}{D^{\ell,r}}, \tag{17a}$$

$$\eta_v^{\ell,r} = \frac{2BH^2M^2(m_h + m_v)}{D^{\ell,r}} + \frac{2BMJ_C(M + m_h + m_v)}{D^{\ell,r}}, \tag{17b}$$

$$\eta_\phi^{\ell,r} = \frac{H^2M(M + m_v)(m_h + m_v)}{D^{\ell,r}} - \frac{(B^2 - e^2)Mm_v(M + m_h + m_v)}{D^{\ell,r}} + \frac{J_C(M + m_v)(M + m_h + m_v)}{D^{\ell,r}}. \tag{17c}$$

where:

$$D^{\ell,r} = H^2M(M + m_v)(m_h + m_v) + (B \pm e)^2Mm_v(M + m_h + m_v) + J_C(M + m_v)(M + m_h + m_v). \tag{18}$$

2.6. Overturning conditions

The failure condition of the system is defined by the overturning of the rigid block. This condition is conventionally assumed to occur when the absolute value of the block's rotation ϕ reaches a critical threshold, namely $\phi = \pm\alpha_{cr_{\ell,r}}$, where $\alpha_{cr_\ell} = \arctan((B + e)/H)$ and $\alpha_{cr_r} = \arctan((B - e)/H)$ (see Fig. 1).

3. Parametric analysis

An extensive parametric analysis is carried out to investigate the influence of the parameters that govern the response of an asymmetric rigid block placed on a double base isolation system, incorporating both horizontal and vertical isolation components.

This study examines rigid block configurations that share the same mass M, moment of inertia about point C (J_C), and identical height H and base width $2B$, but differ in their eccentricity e. It is clear that, if these characteristics are kept constant, changing the eccentricity e inherently means dealing with blocks that have different geometric shapes and/or mass distributions within their volume.

Due to the geometrical properties of the system, its response is identical in the following two cases:

(1) Positive and negative eccentricity ε (or e) of equal magnitude, with fixed base excitation;

Table 1
Geometrical characteristics of the rigid-blocks.

Object	B [m]	H [m]	D [m]	M [kg]	$\lambda[\cdot]$	J_C [kg · m^2]
1	0.175	0.95	0.35	895	5.43	278.38
2	0.3	1.1	1.2	676	3.67	292.93
3	0.19	0.82	0.75	68	4.32	16.06

(2) Positive eccentricity ε (or e) with base excitation multiplied by ± 1.

Owing to this equivalence, the analysis hereafter will consistently consider only the case denoted as (1).

3.1. Reference rigid blocks

While numerical simulations have been performed on various rigid block configurations, the results shown throughout this paper, both in this and subsequent sections, are limited, for conciseness, to blocks sharing the properties listed in Table 1.[1]

Specifically, Object 1 refers to a commercial caryatid with a specific base [36], Object 2 is a server cabinet [37], whereas Object 3 is a hospital cabinet [38]. The mass of the cabinets (Objects 2 and 3) also includes that of the content.

3.2. Variable parameters

Parameters considered variable and characterizing both the isolation devices and the asymmetric block are described below. Specifically:

- Characteristic period of the horizontal isolation device T_h:

$$T_h = 2\pi\sqrt{\frac{M + m_h + m_v}{k_h}}. \tag{19}$$

- Characteristic period of the vertical isolation device T_v:

$$T_v = 2\pi\sqrt{\frac{M + m_v}{k_v}}. \tag{20}$$

- Nondimensional eccentricity $\varepsilon = \frac{e}{B}$.

It is worth observing that the variation of the periods T_h and T_v corresponds to a variation of the stiffnesses k_h and k_v, respectively, since the masses of the system are fixed parameters.

3.3. Fixed parameters

The parameters that are kept fixed, as their variation is not deemed relevant for this study, are listed below. These include:

- Ratio between post-yielding stiffness and pre-yielding stiffness $\psi = 0.25$.
- The yielding displacement is given by

$$u_y = \frac{PGA_h(M + m_h + m_v)}{k_h}\,\alpha_y, \tag{21}$$

with $\alpha_y = 0.1$. Specifically, the yielding displacement u_y corresponds to a fraction α_y of the horizontal elastic displacement of the isolated base under a static acceleration equal to the horizontal Peak Ground Acceleration (PGA_h).
- Masses of the steel plates of the double isolated base are $m_h = m_v =$ 43.3 kg, 254.3 kg, and 100.7 kg for objects 1, 2, and 3, respectively.

[1] The depth parameter D is reported for completeness of the three-dimensional geometric description of the objects. Although D does not explicitly appear in the governing equations, it directly affects the mass M and the centroidal moment of inertia J_C, whose values are explicitly provided in Table 1.

4. Seismic analysis

The results of the parametric analysis are presented using two types of maps. The first are the rocking maps, which are contour plots of the rocking index ζ. This index is defined as the ratio between the maximum absolute rotation $\max|\phi|$ and the critical angle α_{cr_ℓ} or α_{cr_r}. The appropriate critical angle is selected depending on whether the maximum rotation occurs for a positive angle, corresponding to rocking about the left corner, or for a negative angle, which corresponds to rocking about the right corner. These maps are reported in the T_h–T_v parameter space, where the isolated rigid block is subjected to seismic excitation from a recorded earthquake. The rocking maps are divided into three distinct regions:

(i) A dark gray region where $\zeta = 1$, indicating direct overturning of the block;
(ii) A light gray region where $\zeta = 0$, corresponding to a full-contact state in which the block remains attached to the isolated base;
(iii) An intermediate region with a gradient of gray shading from light to dark, representing rocking motion without overturning. The contour levels indicate the maximum value of the rocking index ζ attained during the motion.

In the graphs, the overturning region (dark grey) and the rocking region (shaded grey) are always separated by a thick solid curve, whereas the rocking region and the full-contact region (light grey) is separated by a thick dashed curve.

The second type of maps are the displacement maps, which illustrate contour plots of the maximum absolute horizontal or vertical displacement of the isolated base, i.e., $\max|u|$ or $\max|v|$, within the T_h–T_v parameter space, under seismic excitation from an earthquake record. Based on the direction of the displacement represented, these maps are referred to as horizontal displacement maps or vertical displacement maps, respectively. A grayscale gradient from light to dark is used to visually represent increasing displacement magnitudes, from lower to higher values.

4.1. Earthquake records

A set of three earthquake records, including both horizontal and vertical ground motions, is employed in the seismic analyses. The records were selected based on variations in their spectral properties and peak ground accelerations (PGAs). Fig. 3 shows the time-histories of the horizontal and vertical components of the chosen records. The earthquake records considered are:

(a) Kobe, 1995 Japan earthquake, Takarazuka station, 0 deg, ground level, position of the station: 34.8090N, 135.3440W;
(b) Pacoima, 1971 San Fernando, California earthquake, station no. 279, comp S16E, position of the station: 34.335N, 118.3967W.
(c) Parkfield, 1966 California earthquake, station no. 013, comp N65E, position of the station: 35.726N, 120.287W.

For reference, each record is identified by the underlined name provided in the list above.

4.2. Seismic response under Kobe earthquake

The seismic analyses presented in this section refer to blocks subjected to the Kobe earthquake. The analysis begins with the construction of rocking maps, focusing on Object 1 (see Table 1).

Fig. 4 shows the rocking maps for different values of percentage eccentricity ε, namely $\varepsilon = 0$, $\varepsilon = \pm 20\%$, and $\varepsilon = \pm 40\%$. The first general observation concerns the numerical range of the vertical axis, that is, the range of the vertical period T_v considered in the analyses. The construction of the rocking maps, both here and in the following analyses, is limited to $T_v = 2.0$ s, since for larger values the thick solid and thick

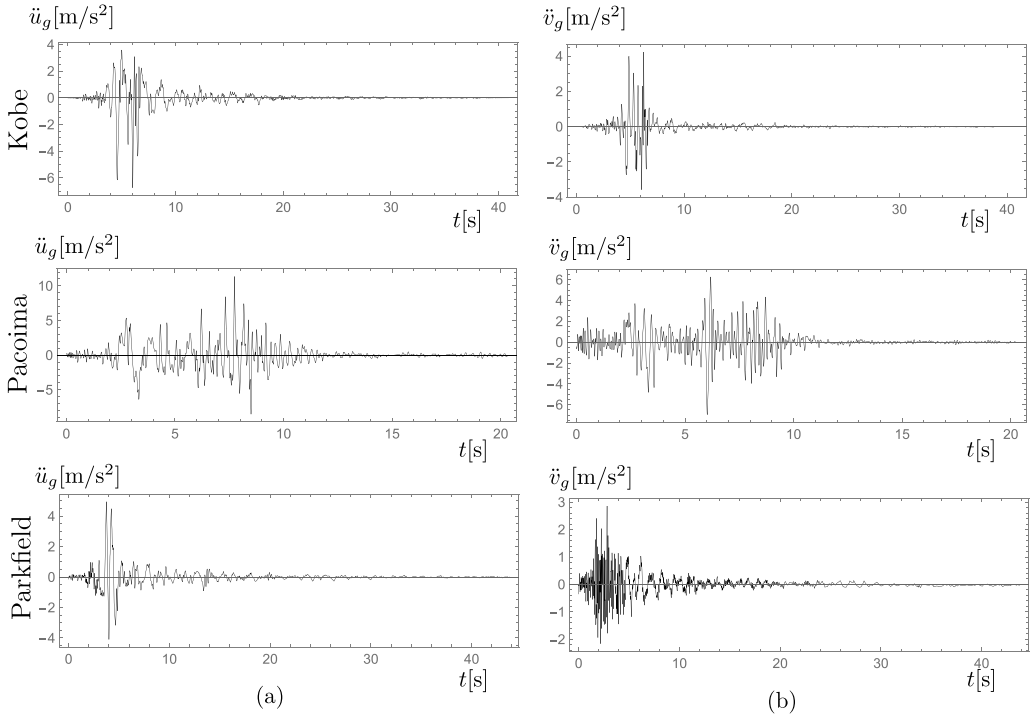

Fig. 3. Seismic excitations: (a) horizontal component; (b) vertical component.

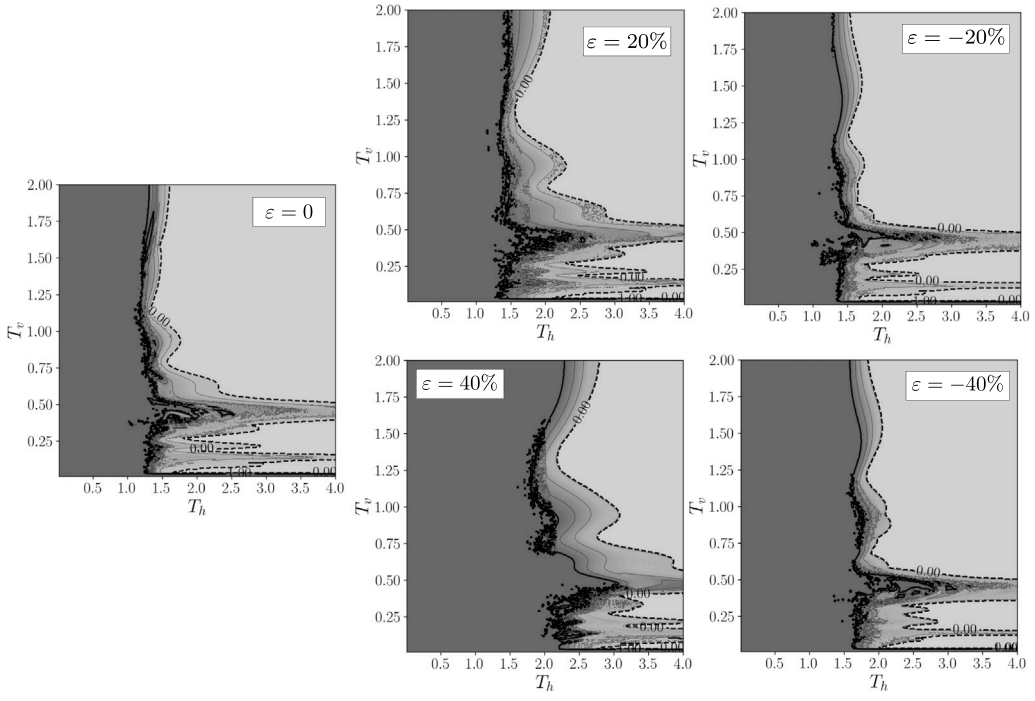

Fig. 4. Rocking maps for Object 1 under Kobe earthquake for different eccentricities ε.

dashed separating curves, as well as the contour levels, tend to become vertical and nearly parallel. Therefore, for $T_v > 2.0$ s, the influence of the vertical isolation period becomes very marginal. Another interesting observation arises from the fact that the thick solid separating curve is nearly vertical in all the rocking maps. This indicates the existence of a horizontal isolation period below which the block is prone to overturning. Therefore, to protect the block, it is necessary to adopt a horizontal isolation period greater than this critical value.

The comparison between the rocking map for the symmetric block ($\varepsilon = 0$, left map) and those for the asymmetric block ($\varepsilon \neq 0$) is particularly insightful. As can be observed, the critical horizontal isolation period above which the block avoids overturning increases with increasing eccentricity. Furthermore, the dynamic behavior of the block can differ noticeably for positive and negative eccentricities. Specifically, the comparison between the cases with $\varepsilon = 0$ and $\varepsilon = \pm 20\%$ shows that for small eccentricities, both positive and negative, there is a slight increase

in the horizontal isolation period from values slightly below 1.5 s to nearly 1.5 s. For larger absolute eccentricities, $\varepsilon = \pm 40\%$, the minimum period required to prevent overturning increases significantly. In addition, a markedly asymmetric behavior emerges, making the block's response quite different for negative versus positive eccentricities.

As a final remark, the region where the block undergoes rocking motion is generally much smaller than the overturning and full-contact regions. Moreover, for certain values of the vertical isolation period T_v, for example $T_v \simeq 0.50$ s, the block never reaches the full-contact conditions regardless of the horizontal isolation period T_h, in contrast to what occurs for many other values of T_v.

A detailed investigation of the rocking maps near the zero value of the vertical isolation period T_v reveals several interesting aspects. Fig. 5 shows a zoomed view of the rocking maps from Fig. 4, focusing on a much smaller range of vertical isolation periods. The behavior of the system at small vertical isolation periods corresponds to a very stiff vertical isolation, approaching the case where vertical isolation is absent ($T_v \to 0$, $k_v \to \infty$). As observed, for very small values of T_v, the block always overturns and never exhibits rocking or full-contact motion. Therefore, it can be concluded that the presence of vertical isolation plays a protective role, preventing the block from overturning. An appropriate choice of the horizontal and vertical isolation periods allows the block to remain in full-contact at all times, effectively avoiding uplift and the onset of rocking motion. For instance, for a block with $\varepsilon = -40\%$, if the pair of isolation periods is chosen at point A (see the right map in Fig. 5), a very small vertical isolation period of $T_v \approx 0.2$ s, combined with the corresponding horizontal isolation, is sufficient to keep the block in full-contact.

The analysis of the horizontal and vertical displacements of the isolated base is a fundamental aspect for evaluating the feasibility of the dual isolation system. Accordingly, horizontal and vertical displacement maps are constructed, each representing a contour plot of the maximum absolute displacements of the dual-isolated base in the same T_h–T_v parameter plane used for the rocking maps. Fig. 6 shows the horizontal (Fig. 6a) and vertical (Fig. 6b) displacement maps for Object 1, with eccentricities $\varepsilon = 0$, $\varepsilon = 40\%$, and $\varepsilon = -40\%$, under the Kobe earthquake. From an initial observation of both displacement maps, the maximum horizontal and vertical displacements of the isolated base are

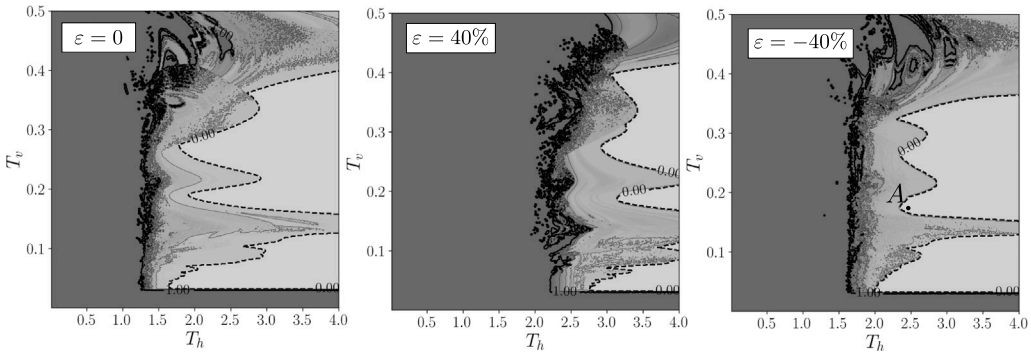

Fig. 5. Zoom of the rocking maps for Object 1 under Kobe earthquake for different eccentricities ε.

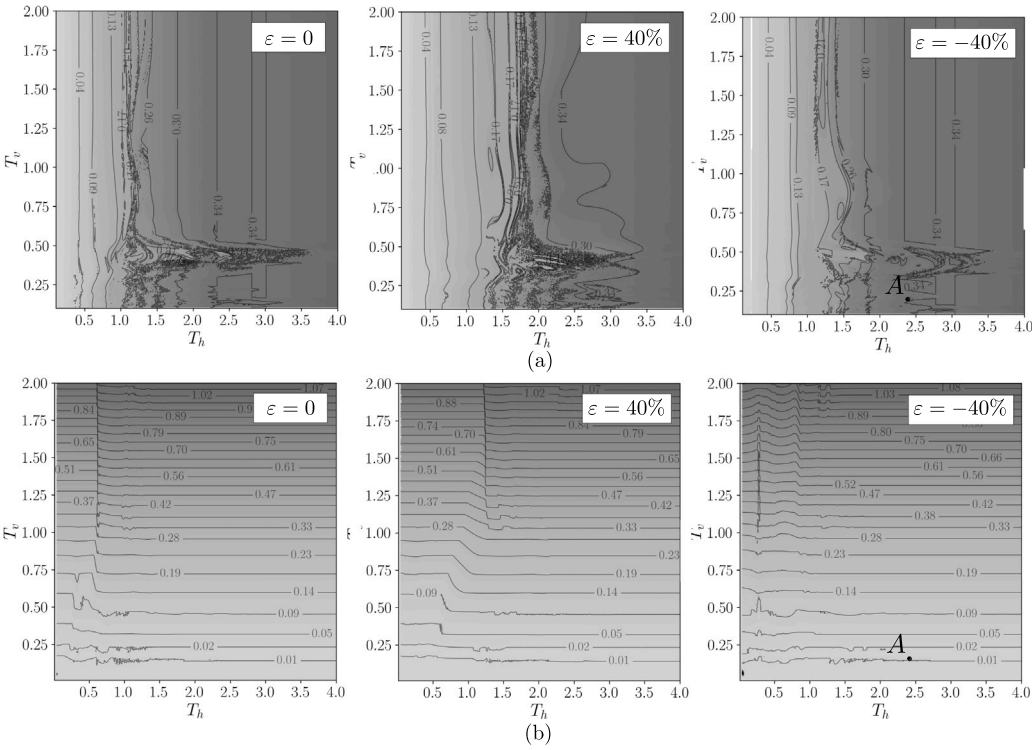

Fig. 6. Displacement maps for Object 1 under Kobe earthquake: (a) horizontal displacement of the isolated base; (b) vertical displacement of the isolated base.

only slightly affected by the eccentricity of the block. Focusing first on the horizontal isolation, it can be observed that the base displacement generally increases with the isolation period T_h, reaching maximum values of about 35 cm, comparable to those observed in isolation systems for frame structures. The contour levels appear almost vertical and parallel to each other, except around the vertical isolation period $T_v \approx 0.5$ s, where a noticeable perturbation occurs. This perturbation takes place within the same parameter range where the rocking maps in Fig. 4 show a rocking region extending over the entire horizontal period range, without ever reaching the full-contact state. This behavior arises because the rocking motion of the block strongly interacts with the horizontal motion of the isolated base. In contrast, the vertical displacement increases very rapidly with the vertical isolation period T_v, reaching values greater than one meter even for moderate isolation periods, such as $T_v = 2.0$ s. The larger vertical displacement is primarily attributed to the static vertical deflection of the isolation device under the self-weight of the block, which becomes increasingly significant as the vertical isolation period increases (i.e., as the vertical stiffness k_v decreases).

The possibility of obtaining effective results even for very small vertical isolation periods, as discussed above, makes it possible to limit the vertical displacement to very small values. For example, point *A*, already shown in Fig. 5, is also reported in the horizontal and vertical displacement maps of the block with $\varepsilon = -40\%$ (right maps in Fig. 6), in order to evaluate the maximum displacements of an isolated base capable of keeping the block in the full-contact state, as previously discussed. As can be observed, the selected very small vertical period leads to vertical displacements on the order of one centimeter.

Finally, Fig. 7 shows the rocking maps of Object 1 under the other two earthquake records, Pacoima (Fig. 7a) and Parkfield (Fig. 7b), for different eccentricities of the block. The same general observations made when discussing the maps in Fig. 4 also apply here. Specifically, for both earthquakes considered, it can be observed that: (*i*) the horizontal isolation period above which the block avoids overturning for any vertical period T_v increases with increasing eccentricity; and (*ii*) a markedly asymmetric behavior emerges, making the block's response quite different for negative and positive eccentricities.

The most interesting aspect arises from the comparison of the maps obtained for the three different earthquakes: Kobe (Fig. 4), and Pacoima and Parkfield (Fig. 7). As can be observed, the worst behavior, characterized by a larger overturning (dark grey) regions, is obtained when the block is excited by the Pacoima earthquake. This occurs because that record exhibits the highest PGA in the vertical ground motion (see Fig. 3). Conversely, the most favorable behavior is observed for the Parkfield earthquake, which shows the lowest vertical PGA. Moreover, the large vertical PGA exhibited by the Pacoima earthquake makes the system more sensitive to the block's eccentricity. In fact, for $\varepsilon = -40\%$, the overturning (dark grey) region extends over almost the entire parameter plane, at least within the ranges investigated in the analysis.

4.3. Seismic response of blocks with varying geometrical and mechanical properties

In this section, the rocking maps of Objects 2 and 3 (see Table 1), subjected to the three selected earthquake records, are presented and discussed. Fig. 8 presents the rocking maps of Object 2 under the Kobe, Pacoima, and Parkfield earthquakes (Figs. 8a–c, respectively), while Fig. 9 illustrates the corresponding maps for Object 3 under the same earthquake records (Figs. 9a–c, respectively).

For both Object 2 and Object 3, and for all the selected earthquake records, it can be observed that: (*i*) the horizontal isolation period above which the block avoids overturning for any vertical period T_v increases with increasing eccentricity; and (*ii*) a markedly asymmetric behavior emerges, making the block's response distinctly different for negative and positive eccentricities. The worst performance, corresponding to the largest overturning region (dark grey), is consistently associated with the Pacoima earthquake, which exhibits the highest vertical PGA, whereas the best performance, corresponding to the smallest overturning region, is obtained under the Parkfield earthquake, characterized by the lowest vertical PGA.

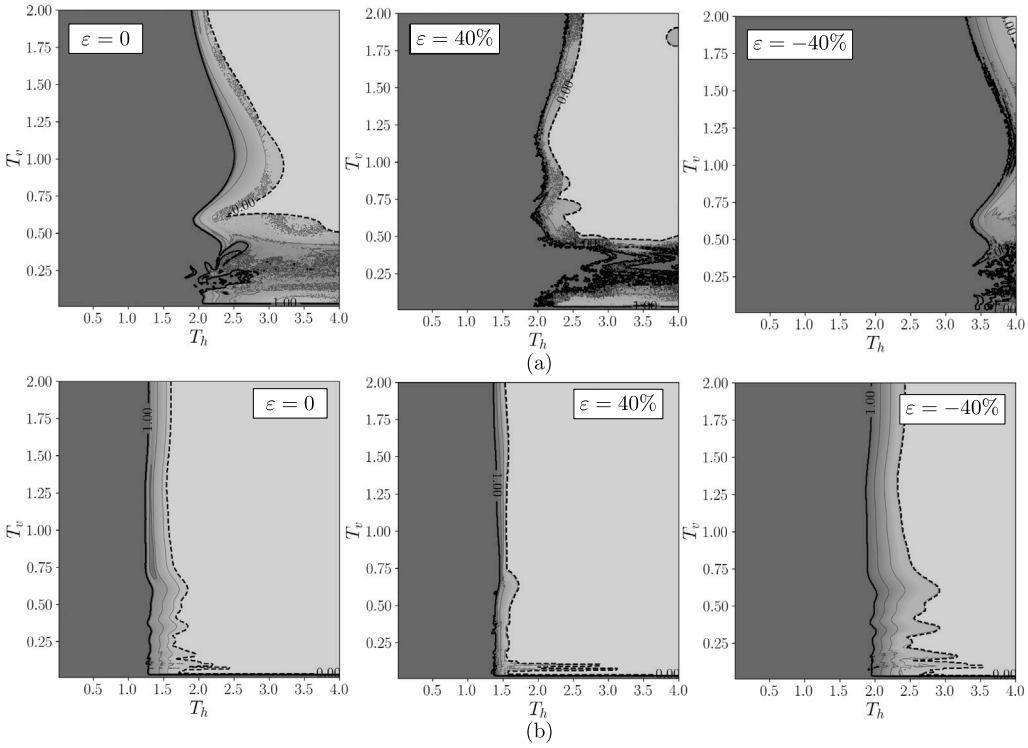

Fig. 7. Rocking maps for Object **1** and different eccentricities ε: (a) Pacoima earthquake; (b) Parkfield earthquake.

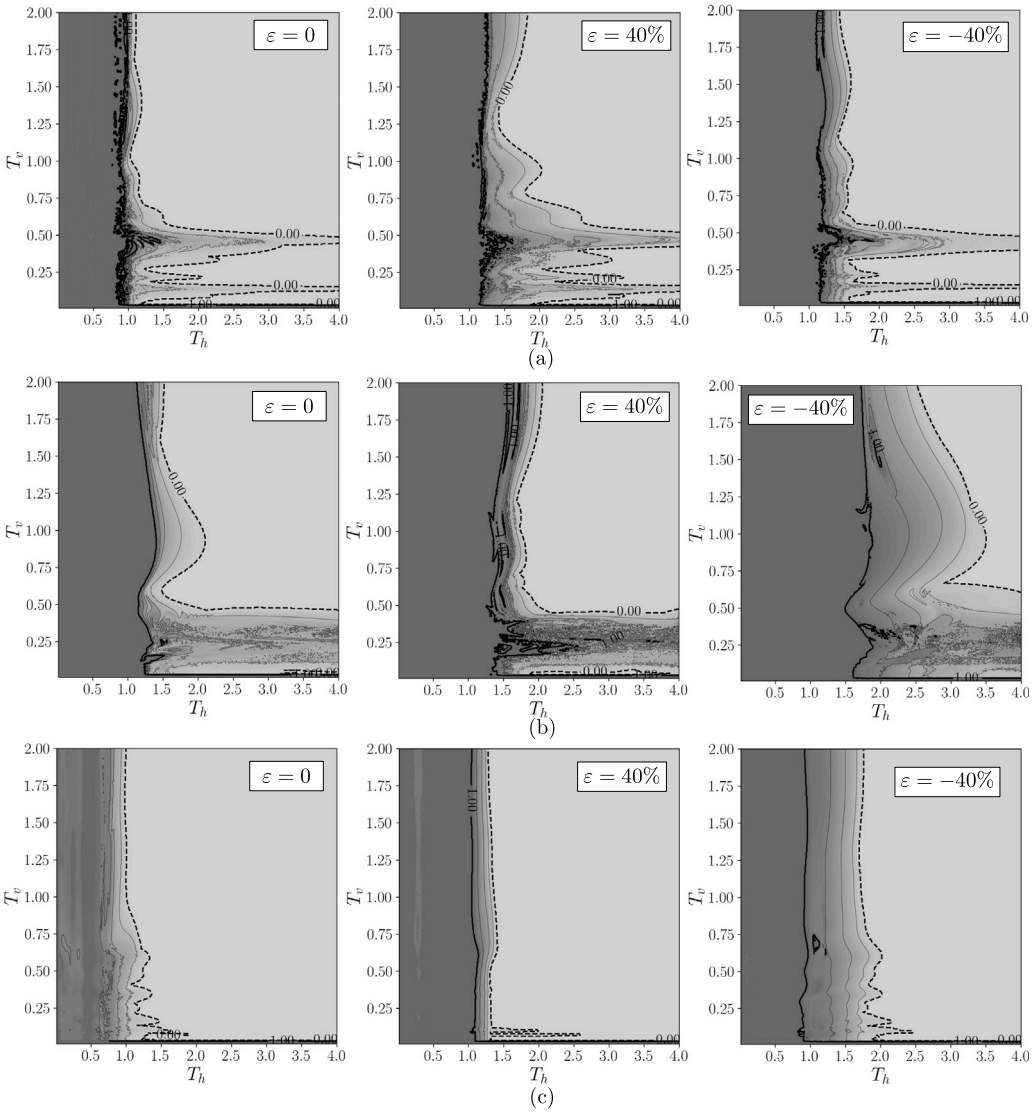

Fig. 8. Rocking maps for Object 2 and different eccentricities ε: (a) Kobe earthquake; (b) Pacoima earthquake; (c) Parkfield earthquake.

By comparing the rocking maps of Objects 1, 2, and 3 (Figs. 4 and 7–9, respectively), it can be observed that Object 1 exhibits the poorest performance under the selected earthquakes, whereas Object 2 shows the best behavior. Object 1 is characterized by the largest overturning regions, while these regions are significantly smaller for Object 2. In particular, when Object 2, with an eccentricity of $\varepsilon = 0$, is excited by the Parkfield earthquake (see the lower-left rocking map in Fig. 8), the overturning region becomes very small. Nevertheless, there exist extended rocking regions where the rocking index is very close to 1, indicating that the block reaches near-overturning conditions even though it does not fully overturn. Summarizing these results, it can be observed that the slenderness of the dual isolated block plays a fundamental role, as higher slenderness is associated with poorer performance, whereas lower slenderness corresponds to better seismic behavior.

5. Overturning spectra

As reported in [39], a symmetric rigid block, not supported by any isolation system and subjected solely to a horizontal one-sine impulsive input, was found to collapse through only two distinct mechanisms: (*i*) overturning following a single impact with the base, or (*ii*) overturning without undergoing any impact.

In this section, a study is undertaken to determine the collapse modes of an asymmetric rigid block resting on a dual base isolation system, expanding upon the findings presented in [39]. The excitation at the base is represented by a one-sine impulsive acceleration, applied simultaneously in the horizontal and vertical directions. Its analytical expression is given by:

$$\ddot{u}_g(t) = \begin{cases} A_h \sin(\Omega t), & 0 \le t < T_S, \\ 0, & T_S < t < t_{max}, \end{cases} \tag{22a}$$

$$\ddot{v}_g(t) = \begin{cases} A_v \sin(\Omega t), & 0 \le t < T_S, \\ 0, & T_S < t < t_{max}. \end{cases} \tag{22b}$$

Here, $T_S = 2\pi/\Omega$ denotes the period of the one-sine wave, A_h and A_v represent the amplitudes in the horizontal and vertical directions, respectively, and t_{max} corresponds to the total duration of the numerical simulation, which is assumed to be greater than 30 s. The eccentricity is varied between positive and negative values, according to Section 3. A graphical depiction of the one-sine impulse is shown in Fig. 10.

A comprehensive parametric analysis is performed by varying the horizontal amplitude A_h and the circular frequency Ω of both the single-cycle horizontal and vertical sine pulses, while keeping the vertical amplitude A_v and the isolation periods T_h and T_v constant. The objective

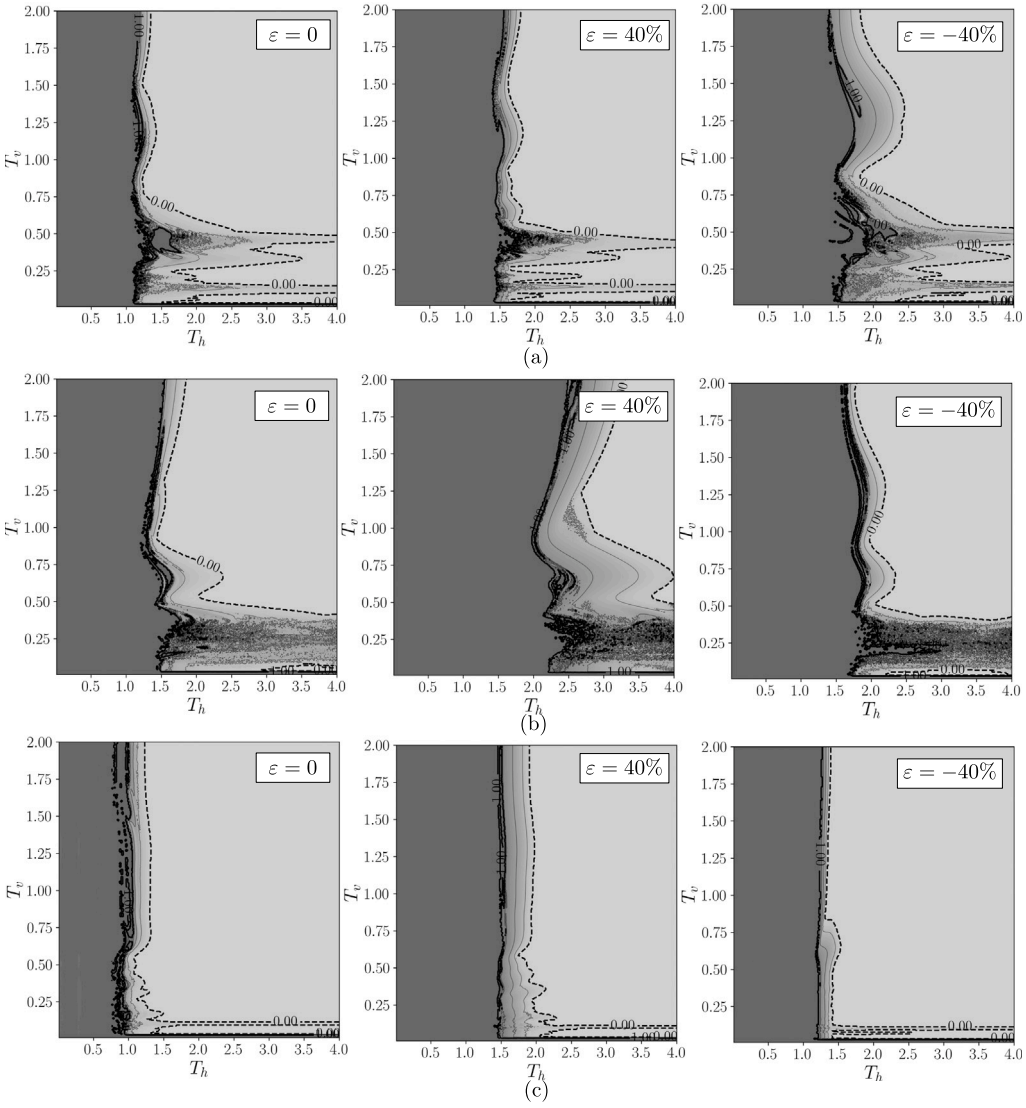

Fig. 9. Rocking maps for Object 3 and different eccentricities ε: (a) Kobe earthquake; (b) Pacoima earthquake; (c) Parkfield earthquake.

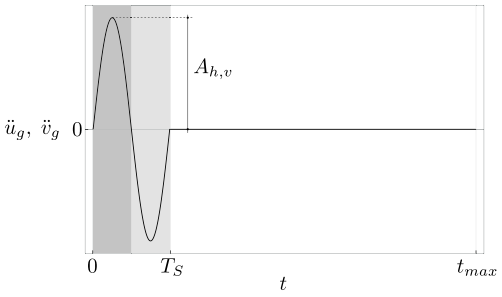

Fig. 10. One-sine impulsive excitation.

is to determine, for each combination of (A_h, Ω), whether the asymmetric block remains dynamically stable during rocking (i.e., the block does not overturn), or, if overturning occurs, to identify the number of impacts preceding collapse. The classification of the block's dynamic response is obtained through numerical integration of the nonlinear equations of motion governing the asymmetric rigid block.

The corresponding results are presented in the form of overturning spectral maps. Distinct regions in the maps are color-coded, each representing a specific overturning pattern observed in the numerical simulations. For instance, green areas denote stable rocking without collapse; blue indicates overturning after a single impact with the base; and red marks overturning that occurs without any intermediate impact. Additional collapse mechanisms, not included in these categories, are shown in other colors as specified in the legend. Particular attention is devoted to the analysis of collapse patterns exhibiting dynamic features not previously documented in the literature.

5.1. Positive value of eccentricity

Following the procedure described in Section 3, the overturning spectral maps are constructed for both positive and negative eccentricities ε of the block. In this section, the rocking spectral maps obtained for positive eccentricities ($\varepsilon > 0$) are first discussed.

Fig. 11 shows the rocking spectral maps of Object 1 placed on a dual isolated base with fixed isolation periods $T_h = 1.75$ s and $T_v = 0.75$ s, for different eccentricities and amplitudes A_v of the vertical one-sine impulsive excitation. Specifically, the upper maps correspond to the case without vertical excitation ($A_v = 0$), whereas the lower maps refer to a vertical impulsive amplitude of $A_v = 0.5$ m/s^2. From left to right, the maps correspond to increasing eccentricity values: $\varepsilon = 0$, $\varepsilon = 20\%$, and $\varepsilon = 40\%$.

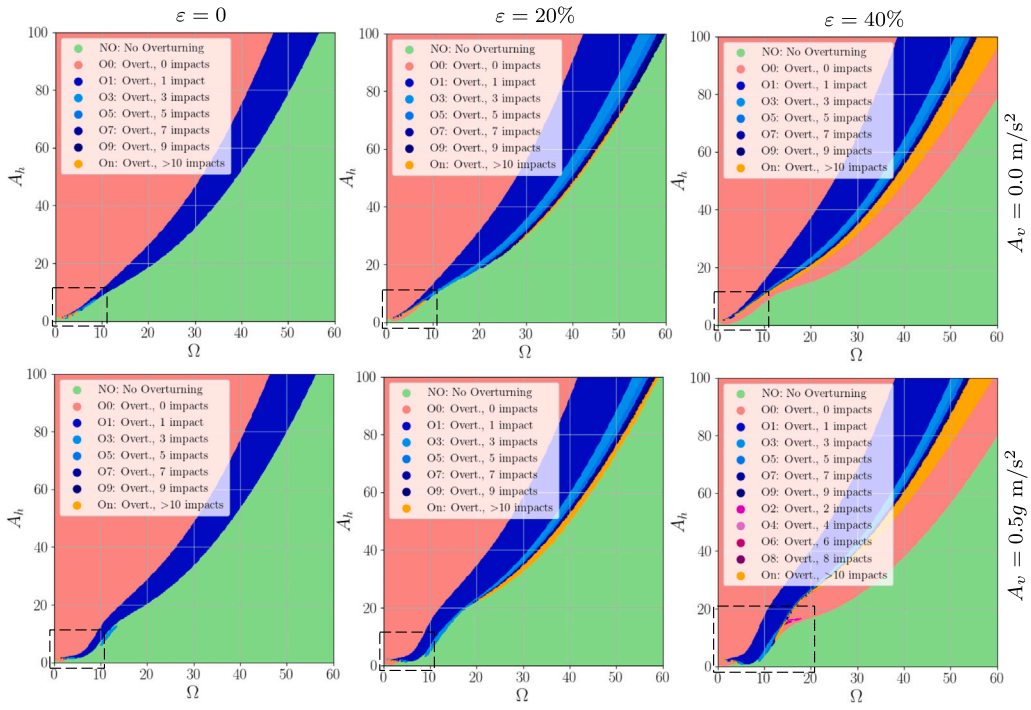

Fig. 11. Overturning spectral maps for null or different positive eccentricities ε of Object 1 and for different vertical one-sine acceleration amplitudes A_v ($T_h = 1.75$ s, $T_v = 0.75$ s).

Starting from the maps obtained in the absence of vertical impulsive excitation (upper maps), the case with $\varepsilon = 0$ (left map) exhibits three predominant overturning regions: the green area, representing stable conditions where no overturning occurs; the blue area, where the block overturns about the right base vertex after a single impact; and the red area, where the block overturns directly about the left base vertex. The legend in the map also indicates the presence of several multi-impact overturning regions, which are not clearly distinguishable in the main maps. This is because such regions are confined to a very narrow range of the varying parameters Ω and A_h. A zoomed-in view of the dashed windows near the origin of the axes would allow these regions to be revealed more clearly.

An increase in eccentricity from $\varepsilon = 20\%$ (middle map) to $\varepsilon = 40\%$ (right map) enlarges the multi-impact overturning regions, making them more clearly distinguishable. Moreover, below these multi-impact regions, a new red area appears, corresponding to overturning directly about the right base vertex without any intermediate impact. This region differs from the upper red one in the vertex about which the overturning occurs. The size of this new red region increases with increasing eccentricity. For $\varepsilon = 20\%$, it is large enough to be visible only within the dashed window near the origin, whereas for $\varepsilon = 40\%$, it becomes sufficiently extended to be clearly recognizable across the entire parameter plane. The introduction of the vertical one-sine impulsive excitation with $A_v = 0.5\text{m/s}^2$ (lower maps) slightly distorts the overturning regions, mainly near the origin of the axes, and generally leads to a modest enlargement of both the new red region and the multi-impact overturning regions.

Referring to the study by the same authors in [29], where the overturning behavior of asymmetric rigid blocks on a fixed support was investigated, it was found that multiple-impact overturning regions also appear due to the block's eccentricity; however, they always remain confined to a very small area near the origin of the axes. In contrast, when both the dual isolation system and the block asymmetry coexist, the size of the multi-impact regions becomes highly sensitive to the eccentricity, increasing significantly as ε grows. Finally, from the legend of the lower-right map, it can be observed that the combined effect of the vertical impulsive excitation and the block eccentricity leads to the appearance of multi-impact regions characterized by both odd and even numbers of impacts. This result represents a novel finding compared to the case of the asymmetric block on a fixed support, where, for positive eccentricity and a horizontal one-sine impulsive excitation with positive amplitude, only multi-impact regions with an odd number of impacts, along with the 0-impact (red) regions, were observed. It is worth noting that in the odd-impact regions, overturning always occurs about the right base vertex, whereas in the even-impact regions, overturning always occurs about the left base vertex.

To conclude, an increase in the eccentricity ε leads to a general reduction in the size of the green stable region, and consequently to an overall deterioration of the block's safety.

To gain deeper insights into the nature of the multi-impact regions around the origin of the axes, the zoomed-in views of the dashed windows in the maps of Fig. 11 are presented in Fig. 12. The upper maps correspond to the case without the vertical one-sine impulsive excitation. The influence of the increasing eccentricity is evident: from the left ($\varepsilon = 0$) to the right ($\varepsilon = 40\%$) maps, passing through the middle one with intermediate eccentricity ($\varepsilon = 20\%$), a progressive enlargement of the new lower red 0-impact region, as well as of the several multi-impact overturning regions, can be observed. Moreover, the higher level of detail provided by the zoomed-in views makes it possible to identify the presence of multi-impact regions with both odd and even numbers of impacts before overturning. The presence of the vertical one-sine impulsive excitation (lower maps) modifies the shape and the size of the overturning region and increases the number of distinct multi-impact regions observable within the same parameter range (see the legends of the lower maps in comparison with those of the upper maps).

As observed in the zoomed-in views in Fig. 12, a particularly interesting feature emerges: there always exists a range of one-sine excitation frequencies for which overturning occurs at lower excitation amplitudes.

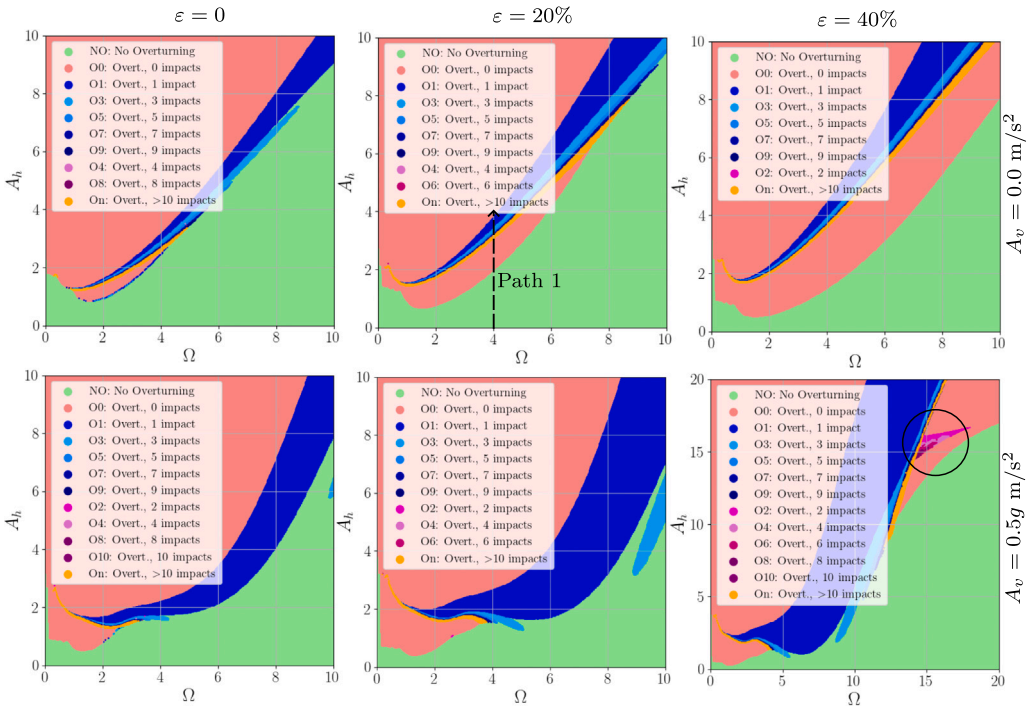

Fig. 12. Zoom-in of the overturning spectral maps for null or different positive eccentricities ε of Object 1 and for different vertical one-sine acceleration amplitudes A_v ($T_h = 1.75$ s, $T_v = 0.75$ s).

This represents a novel behavior, directly related to the vertical motion of the dual isolated base. In contrast, for non-isolated blocks, the overturning amplitude of the one-sine impulse increases monotonically with the excitation frequency.

Along Path 1 shown in the upper-middle map of Fig. 12, proceeding from bottom to top, one first encounters the red 0-impact region with overturning about the right base vertex. Immediately afterward, the path crosses the multi-impact region, where the number of impacts before overturning decreases progressively from a very high value toward the top. Continuing upward, the path reaches the one-impact blue region, and finally the red 0-impact region with overturning about the left base vertex.

The interpretation of the main overturning modes encountered along Path 1 is listed below:

- Inside the lower red 0-impact region, overturning occurs about the right base vertex because the first half-wave of the one-sine impulse does not have sufficient amplitude to uplift the block around the left base vertex, causing the block to remain in full contact during this first half-wave. On the other hand, due to the block's asymmetry, the second half-wave of the excitation uplifts the block around the right base vertex, leading to overturning.
- The Path 1 crosses only multi-impact overturning regions with an odd number of impacts before the overturning of the block. Inside such regions, overturning occurs after a number of impacts that decrease progressively from a very high value down to one. This happens because the first half-wave of the one-sine impulse is able to uplift the block around the left base vertex, initiating the rocking motion. The amplitude of the rocking motion depends directly on the amplitude of the one-sine impulsive excitation. For very small excitation amplitudes, the resulting rocking angles are also small, and many rocking oscillations occur before the arrival of the second half-wave. Due to the block's asymmetry, the second half-wave overturns the block about the right base vertex. Moving upward along Path 1, the increase in the amplitude of the one-sine impulsive excitation produces a higher initial rocking amplitude, and consequently fewer impacts before the second half-wave of the excitation arrives.
- Finally, inside the upper red 0-impact region, the block overturns without impacting the support around the left base vertex ℓ. This occurs because the first half-wave of the one-sine pulse directly uplifts and overturns the block about the left base vertex.

As discussed above, the overturning spectral maps also display regions characterized by an even number of impacts occurring before the block overturns. Such regions are generally very small and not easily visible in the maps. It is worth noting that these even-overturning modes do not appear among the overturning modes of asymmetric blocks on a fixed support with positive eccentricity and excited only by a horizontal one-sine input with positive amplitude (see [29]).

The present results indicate that the existence of these regions does not depend on the presence of the vertical one-sine impulsive excitation, as they are observed in the zoomed-in views of the asymmetric block for any eccentricity, even in the absence of the vertical excitation (see the upper maps of Fig. 12). However, their size is so small that they are not visible within the selected zoomed-in parameter window. Only at high eccentricities, and in the presence of the vertical one-sine impulsive excitation, do these even-overturning regions enlarge sufficiently to become visible in the selected zoomed-in window (see the magenta shaded region within the circle in the lower-right map of Fig. 12). They are a direct consequence of the vertical motion of the dual isolated base, which is present even in the absence of vertical excitation. This motion interferes with the rocking response, introducing a perturbation that can either reduce or increase the number of impacts experienced by the block before overturning. In fact, the vertical motion of the system directly influences the total vertical acceleration acting on the block, thereby modifying the restoring moments (see Section 2.4). Such effects become more significant, and thus visible over a wider parameter range, for higher eccentricities and, in particular, in the presence of vertical excitation.

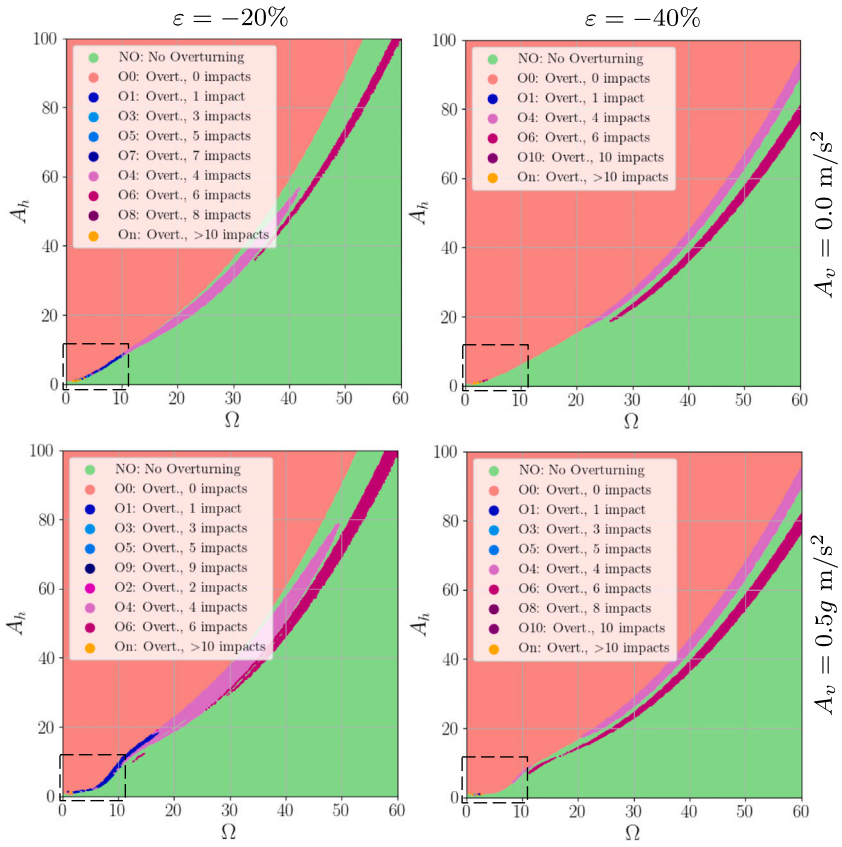

Fig. 13. Overturning spectral maps for different negative eccentricities ε of Object 1 and for different vertical one-sine acceleration amplitudes A_v ($T_h = 1.75$ s, $T_v = 0.75$ s).

5.2. Negative value of eccentricity

In this section, the rocking spectral maps obtained for negative eccentricities ($\varepsilon < 0$) are discussed.

Fig. 13 shows the rocking spectral maps of Object 1 placed on a dual isolated base with fixed isolation periods $T_h = 1.75$ s and $T_v = 0.75$ s, for different eccentricities and amplitudes A_v of the vertical one-sine impulsive excitation. Specifically, the upper maps correspond to the case without vertical excitation ($A_v = 0$), whereas the lower maps refer to a vertical impulsive amplitude of $A_v = 0.5$ m/s^2. From left to right, the maps correspond to decreasing negative eccentricity values, namely $\varepsilon = -20\%$ and $\varepsilon = -40\%$. The maps corresponding to $\varepsilon = 0$ are the same as those reported in Fig. 11 (specifically, the left-hand maps).

Focusing first on the case without vertical excitation, it can be observed from the upper-left map of Fig. 11 and the upper maps of Fig. 13 that decreasing the eccentricity from $\varepsilon = 0$ to $\varepsilon = -40\%$ causes a significant reduction in the size of the blue region corresponding to overturning after one impact. At the same time, new multi-impact regions emerge, predominantly characterized by an even number of impacts before overturning. These even multi-impact overturning regions only slightly depend on the decrease in eccentricity (compare the two upper maps in Fig. 13). The presence of the vertical one-sine impulsive excitation, as shown in the lower-left map of Fig. 11 and the lower maps of Fig. 13, does not qualitatively alter the situation previously described for $A_v = 0$, but it slightly affects the size and shape of the even multi-impact overturning regions. However, negative eccentricity generally reduces the size of the odd multi-impact overturning regions while enlarging the regions with even multi-impacts before overturning. As can be observed from the legends of the maps in Fig. 13, several other regions, where overturning occurs after both even and odd impacts, coexist in the same parameter plane, although many of them are too small to be easily visible.

To conclude, even for negative eccentricities, a decrease in ε leads to a general reduction in the size of the green stable region and, consequently, to an overall deterioration of the block's safety.

To investigate more thoroughly the nature of the several multi-impact overturning regions that are not visible within the parameter ranges used to construct the previous maps, zoomed-in views of the dashed windows near the axis origin, as indicated in the maps of Fig. 13, are presented in Fig. 14. Even at a small scale of observation, the zoomed-in overturning maps reveal very small multi-impact overturning regions, primarily indicated by the legends in the maps. A further enlargement of the visualization window, obtained through a zoomed-in view of the dashed window in the middle-right map, provides additional details of these multi-impact regions. The lower map in Fig. 14 shows this further zoomed-in view. As observed, the size and shape of these overturning regions are highly complex. Following the evolution of the multi-impact overturning regions along Path 2, the number of impacts, always even except for the blue one-impact overturning region, initially reaches very high values that decrease along the upward path. However, this and other similarly complex scenarios occur at a very small scale, rendering them primarily of academic interest and of little practical relevance in a technical context.

Finally, similarly to the case of positive eccentricity, for negative eccentricity there also exists a range of one-sine excitation frequencies at which overturning occurs at lower excitation amplitudes.

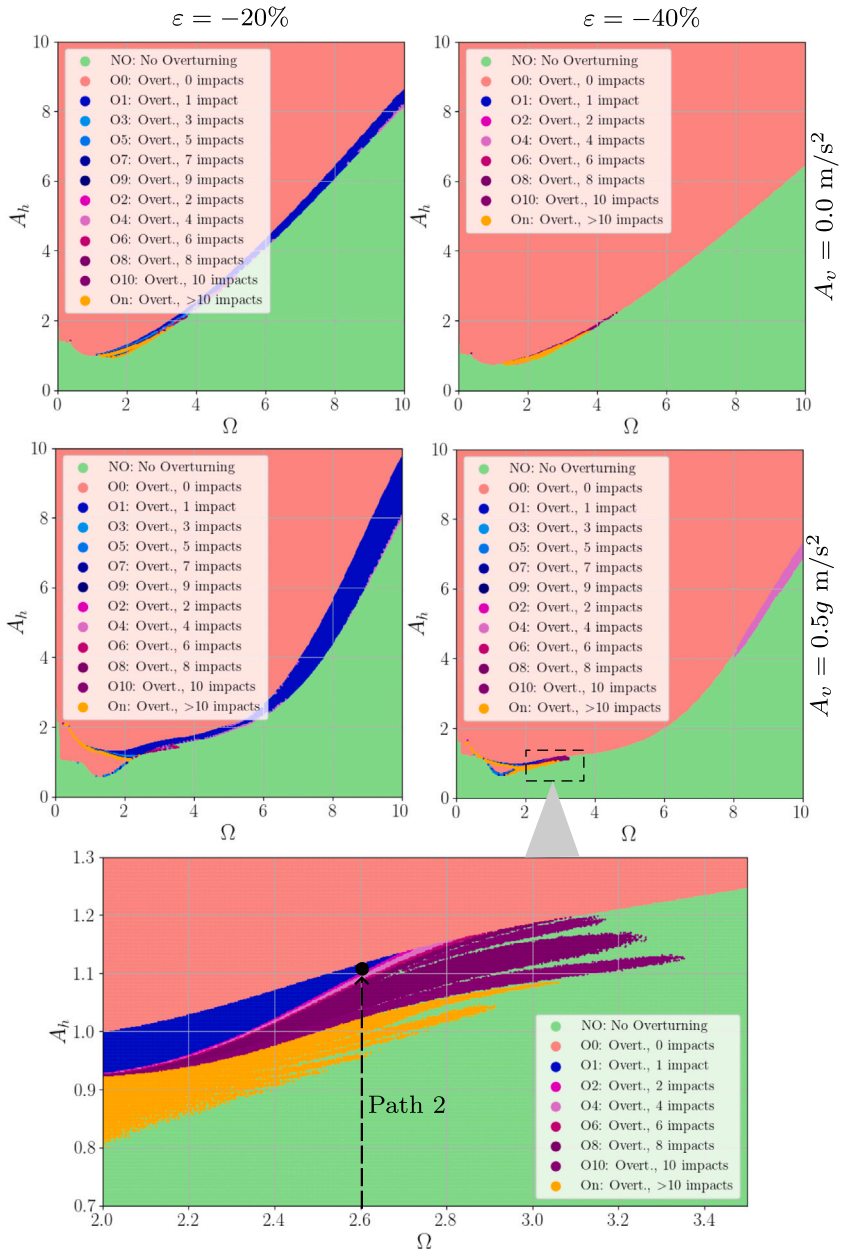

Fig. 14. Zoom-in of the overturning spectral maps for different negative eccentricities ε of Object 1 and for different vertical one-sine acceleration amplitudes A_v ($T_h = 1.75$ s, $T_v = 0.75$ s).

6. Conclusions

This paper presents a comprehensive investigation into the dynamic and seismic behavior of asymmetric rigid blocks supported by a dual base isolation system, consisting of horizontal and vertical isolation devices. The study extends prior research on symmetric blocks with base isolation and asymmetric blocks on fixed bases by combining the two approaches into a unified framework. A refined dynamic model was developed, rigorously accounting for the eccentricity between the geometric and mass centers of the block. The block was assumed to be non-sliding, and only full-contact and rocking motions were considered. The equations of motion, along with uplift and impact conditions, were derived exactly for asymmetric configurations.

Numerical analyses were conducted to investigate both the rocking response and the overturning mechanisms of various asymmetric block geometries. Specifically, three reference rigid blocks were considered, representing a server cabinet, hospital equipment, and a caryatid. The system was subjected to both recorded seismic excitations and impulsive one-sine base accelerations, including horizontal and vertical components. Earthquake records were used to characterize the seismic response and behavior of dual-isolated asymmetric rigid blocks, whereas the characterization of the overturning mechanism required one-sine base excitations. Rocking and overturning spectral maps were obtained to assess the influence of key system parameters, such as the characteristic isolation periods and eccentricity, under seismic and one-sine impulsive excitations, respectively. Finally, the presence of asymmetry introduces a directional dependence in the dynamic response. The rocking equations, along with the uplift and impact conditions, differ between the left and right base corners, resulting in asymmetric rocking motions.

The main findings of the seismic analysis are:

- When both horizontal and vertical seismic components are considered, the dual (horizontal + vertical) base isolation system

enhances the ability of asymmetric blocks to maintain full contact with the base during seismic events. Compared to horizontal-only isolation, the dual system reduces the extent of the overturning regions in the rocking maps.
- The effectiveness of dual isolation increases with longer horizontal isolation periods and is particularly advantageous under earthquakes with high horizontal and vertical peak ground accelerations (PGA). However, beyond a certain threshold of the vertical isolation period, further increases have negligible impact on the system's response.

The main findings in the characterization of the overturning modes are:

- Dual-isolated asymmetric rigid blocks with positive eccentricity, and positive amplitude of the one-sine excitation, exhibit a rich variety of overturning scenarios not previously reported. These include multiple regions characterized by either an odd or even number of impacts before overturning, with the structure becoming increasingly complex at finer excitation scales.
- The same asymmetric rigid blocks without isolation exhibit only overturning scenarios characterized by an odd number of impacts before overturning.
- Dual-isolated asymmetric rigid blocks with negative eccentricity, and positive amplitude of the one-sine excitation, also display a rich variety of overturning scenarios not previously reported, including multiple regions characterized by an odd or even number of impacts before overturning.
- In general, the size of the multiple-impact overturning regions for blocks with negative eccentricity is smaller than that for blocks with positive eccentricity.
- For blocks with both positive and negative eccentricity, there always exists a range of one-sine excitation frequencies for which overturning occurs at lower excitation amplitudes. Such a critical range does not exist for non-isolated blocks with the same geometrical characteristics. Specifically, for non-isolated blocks, the overturning amplitude of the one-sine impulse increases monotonically with increasing excitation frequency.

Overall, this study highlights the complex interplay between asymmetry and multi-directional base isolation in determining the seismic response of rigid blocks and characterizing the overturning modes. The proposed modeling framework and the resulting insights can inform the design of more effective isolation strategies for protecting valuable or sensitive freestanding rigid objects under seismic loading.

CRediT authorship contribution statement

Lorenzo Amoroso: Writing – review & editing, Writing – original draft, Visualization, Validation, Software, Methodology, Investigation. **Manuel Ferretti:** Writing – review & editing, Writing – original draft, Visualization, Validation, Supervision, Software, Methodology, Investigation, Conceptualization. **Angelo Di Egidio:** Writing – review & editing, Writing – original draft, Visualization, Validation, Supervision, Software, Methodology, Investigation, Conceptualization.

Declaration of competing interest

The authors declare that they have no known competing financial interests or personal relationships that could have appeared to influence the work reported in this paper.

Acknowledgments

This work is funded by the European Union - Next Generation EU, Mission 4, Component 2, Investment 1.1, within the framework of the project PRIN 2022, "2022TH5HC2 - Engineered basements for vibration protection of artworks and strategically sensitive equipment" (CUP: E53D2300373 0006, University of L'Aquila).

References

[1] Housner GW. The behaviour of inverted pendulum structures during earthquakes. Bull Seismol Soc Am 1963;53(2):404–17.
[2] Spanos PD, Koh A-S. Rocking of rigid blocks due to harmonic shaking. J Eng Mech 1984;110(11):1627–42.
[3] Tso WK, Wong CM. Steady state rocking response of rigid blocks part 1: analysis. Earthq Eng Struct Dyn 1989;18(1):89–106.
[4] Yim SCS, Lin H. Nonlinear impact and chaotic response of slender rocking objects. J Eng Mech 1991;117(9):2079–100.
[5] Masi F, Stefanou I, Vannucci P, Maffi-Berthier V. Rocking response of inverted pendulum structures under blast loading. Int J Mech Sci 2019;157:833–48.
[6] Ishiyama Y. Motions of rigid bodies and criteria for overturning by earthquake excitations. Earthq Eng Struct Dyn 1982;10(5):635–50.
[7] Shenton III HW, Jones NP. Base excitation of rigid bodies. I: formulation. J Eng Mech 1991;117(10):2286–306.
[8] Lipscombe P, Pellegrino S. Free rocking of prismatic blocks. J Eng Mech 1993;119:1387–410.
[9] Mathey C, Feau, C, Politopoulos, I, Clair, D, Baillet, L, Fogli, M. Behavior of rigid blocks with geometrical defects under seismic motion: an experimental and numerical study. Earthq Eng Struct Dyn 2016;45(15):2455–2474.
[10] Charalampakis A, Tsiatas G, Tsopelas P. Rocking of rigid blocks: analytical solution and exact energy-based overturning criteria. [arXiv preprint] arXiv:2106.11741. 2021.
[11] Kavvadias IE, Papachatzakis GA, Bantilas KE, Vasiliadis LK, Elenas A. Rocking spectrum intensity measures for seismic assessment of rocking rigid blocks. Soil Dyn Earthq Eng 2017;101:116–24.
[12] Zulli D, Contento A, Di Egidio A. Three-dimensional model of rigid block with a rectangular base subject to pulse-type excitation. Int J Non-Linear Mech 2012;47:679–87.
[13] Di Egidio A, Zulli D, Contento A. Comparison between the seismic response of 2d and 3d models of rigid blocks. Earthq Eng Eng Vib 2014;13:151–62.
[14] D'Angela D, Contento A, Kampas G, Magliulo G. Seismic response of rocking-dominated nonstructural elements: a comprehensive review. J Earthq Eng 2025:1–33.
[15] Contento A, Di Egidio A, Pagliaro, S. Dynamic and seismic protection of rigid-block-like structures with combined dynamic mass absorbers. Eng Struct 2020;272:114999.
[16] Di Egidio A, Contento A. Improvement of the dynamic and seismic behaviour of rigid block-like structures with a hysteretic mass damper coupled with an inerter. Appl Sci 2022;12(22):11527. https://doi.org/10.3390/app122211527.
[17] Di Egidio A, Alaggio R, Aloisio A, de Leo AM, Contento A, Tursini M. Analytical and experimental investigation into the effectiveness of a pendulum dynamic absorber to protect rigid blocks from overturning. Int J Non-Linear Mech 2019;115:1–10.
[18] Di Egidio A, de Leo AM, Contento A. The use of a pendulum dynamic mass absorber to protect a trilithic symmetric system from the overturning. Math Probl Eng 2019:4843738. https://doi.org/10.1155/2019/4843738
[19] Di Egidio A, de Leo A, Simoneschi G. Effectiveness of mass-damper dynamic absorber on rocking block under one-sine pulse ground motion. Int J Non Linear Mech 2016. https://doi.org/10.1016/j.ijnonlinmec.2017.10.015
[20] Simoneschi G, Geniola A, de Leo A, Di Egidio A. On the seismic performances of rigid blocks coupled with an oscillating mass working as tmd. Earthq Eng Struct Dyn 2017;46:1453–69.
[21] Calió I, Marletta M. Passive control of the seismic response of art objects. Eng Struct 2003;25:1009–18.
[22] Di Egidio A, Contento A. Base isolation of sliding-rocking non-symmetyric rigid blocks subjected to impulsive and seismic excitations. Eng Struct 2009;31:2723–34.
[23] Vassiliou MF, Makris N. Analysis of the rocking response of rigid blocks standing free on a seismically isolated base. Earthq Eng Struct Dyn 2012;41(2):177–96.
[24] Ferretti M, Di Egidio A. Effectiveness in protecting rigid-block-like objects through horizontal and vertical seismic isolation. Nonlinear Dyn 2024;112:18745–66.
[25] Simoneschi G, Olivieri C, de Leo AM, Di Egidio A. Pole placement method to control the rocking motion of rigid blocks. Eng Struct 2018;167:39–47.
[26] Di Egidio A, Contento A, Olivieri C, de Leo AM. Protection from overturning of rigid block-like objects with linear quadratic regulator active control. Struct Control Health Monit 2020;27:e2598.
[27] Ceravolo R, Pecorelli ML, Zanotti Fragonara L. Semi-active control of the rocking motion of monolithic art objects. J Sound Vib 2016;374:1–16.
[28] Di Egidio A, Olivieri C, Contento A, Pagliaro S. Improving the dynamic and seismic behaviour of rigid block-like elements through active mass dampers. Eng Struct 2023;275:115312.
[29] Ferretti M, Amoroso L, Di Egidio A. Characterization of the overturning scenario of asymmetric rigid blocks. Eng Struct 2025;341:120790.
[30] de Leo A, Simoneschi G, Fabrizio C, Di Egidio A. On the use of a pendulum as mass damper to control the rocking motion of a non-symmetric rigid block. Meccanica 2016;51:2727–40.
[31] Di Egidio A, Contento A. Seismic response of a non-symmetric rigid block on a constrained oscillating base. Eng Struct 2010;32:3028–39.
[32] Wen Y-K. Method for random vibration of hysteretic systems. J Eng Mech 1976;102(2):249–63.
[33] Rajagopal KR. A note on a reappraisal and generalization of the kelvin-voigt model. Mech Res Commun 2009;36:232–5.

[34] Ma F, Zhang H, Bockstedte A, Foliente GC, Paevere P. Parameter analysis of the differential model of hysteresis. J Eng Mech 2004;71:342–9.
[35] Constantinou MC, Adnane MA. Dynamics of soil-base-isolated structure systems: evaluation of two models for yielding systems. Report to NSAF, Department of civil engineering, Drexel University, Philadelphia 1987.
[36] https://www.recuperando.com/it/statue/12447-erma-pietra-ercole-neoclassico-cariatide.html.
[37] Zhang X, Li Z, Sun G, Zhang P, Zuo H, Shang Q, Wang T. Evaluation of seismic response of server cabinets through shaking table tests. Eng Struct 2024;301:117322.
[38] Di Sarno L, Magliulo G, D'Angela D, Cosenza E. Experimental assessment of the seismic performance of hospital cabinets using shake table testing. Earthq Eng Struct Dyn 2019;48(1):103–23.
[39] Zhang J, Makris N. Rocking response of free-standing blocks under cycloidal pulses. J Eng Mech 2001;127(5):473–83.